Carbon 124 (2017) 357–371

Contents lists available at ScienceDirect

Carbon

journal homepage: www.elsevier.com/locate/carbon

Synchrotron X-ray characterization of crack strain fields in polygranular graphite

S.M. Barhli [a, *], L. Saucedo-Mora [a, b], M.S.L. Jordan [a], A.F. Cinar [c], C. Reinhard [d], M. Mostafavi [e], T.J. Marrow [a]

[a] Department of Materials, University of Oxford, Oxford, OX1 3PH, UK
[b] Institute Eduardo Torroja for Construction Sciences, Serrano Galvache 4, Madrid, 28033, Spain
[c] Department of Materials, University of Sheffield, Sheffield, S1 3JD, UK
[d] Diamond Light Source, Harwell Science and Innovation Campus, Oxfordshire, UK
[e] Department of Mechanical Engineering, University of Bristol, Bristol, BS8 1TR, UK

ARTICLE INFO

Article history:
Received 10 May 2017
Received in revised form
29 August 2017
Accepted 30 August 2017
Available online 3 September 2017

ABSTRACT

The strain field of a crack in polygranular isotropic nuclear graphite, a quasi-brittle material, has been studied during stable fracture propagation. Synchrotron X-ray computed tomography and strain mapping by diffraction were combined with digital volume correlation and phase congruency image analysis to extract the full field displacements and elastic crystal strains. The measured displacement fields have been analysed using a Finite Element method to extract the elastic strain energy release rate as a J-integral. Non-linear properties described the effect of microcracking on the elastic modulus in the fracture process zone. The analysis was verified by the good agreement of the predicted and measured elastic strain fields when using the non-linear model. The intrinsic critical elastic strain energy release rate for mode I crack propagation is approximately 200 J m^{-2}.

1. Introduction

Isotropic polygranular graphite is used in the UK's advanced gas cooled (AGR) nuclear fission reactors as a neutron moderator and reflector. These are load-bearing components, keyed in a structure that forms the reactor core [1,2]. Their integrity is critical to the safe operation of the reactor. Some future high temperature nuclear fission reactor systems will also employ polygranular graphite in structural components [3]. Dimensional change of the graphite, caused by fast neutron irradiation and thermal gradients, can develop tensile stresses that have the potential to cause fracture [2]. An improved understanding and knowledge of the criteria for crack initiation and propagation in graphite under different stress states is important to support the structural integrity assessment of these graphite components [4].

Graphite is generally treated as a linear elastic material and its structural integrity is assessed using linear elastic fracture mechanics that assumes brittle fracture [5–8]. This leads to conservative design in non-irradiated graphite at least, as it is a quasi-brittle material that can exhibit non-linear mechanical behaviour [9,10], development of permanent set after straining [11] and a rising fracture resistance (J-R curve) with crack propagation [10]. Reports of the latter are quite variable and appear to depend on the method of study. For instance, two studies in the same grade of coarse grained graphite used an analysis of the full-field displacements to obtain the J-integral [12] and direct measurement of the energy required to extend the crack length [13]; both found a rising R-curve behaviour (i.e. increase in fracture resistance with increasing crack length) that reached a plateau after significant crack growth (>50 mm), but differed by a factor of two. A recent study in a fine grained graphite compared compliance based methods to measure the critical strain energy release rate with a simple linear elastic fracture mechanics calculation of the stress intensity factor [14]. Rising fracture resistance was observed similarly by both analyses with no plateau, though the extent of crack propagation was less than 10 mm in this case. Polygranular graphite also exhibits effects of size and stress state on strength [15], and these are not fully explained by Weibull-type approaches that consider the relative stressed volumes within a strain gradient [16] [17]. It has been proposed that some of these differences may arise from extrinsic factors, such as crack bridging, that may depend on

* Corresponding author.
E-mail address: selim.barhli@materials.ox.ac.uk (S.M. Barhli).

http://dx.doi.org/10.1016/j.carbon.2017.08.075

specimen geometry; these would act to shield the crack tip and reduce the local stress and strain energy field [18]. Mixed mode loading of polygranular graphite was also investigated [5,19] in notched graphite samples where a strain energy density criterion was shown to be suitable to predict the strength of the specimens.

Knowledge of the failure criterion in graphite is required to resolve these issues, as well as better observations of the stresses and strains that develop in graphite during mechanical loading.

Displacement field mapping by both DIC and the related technique of electronic speckle pattern interferometry (ESPI) has been employed for the early detection and study of fracture nuclei in polygranular graphite [20–23], to which the strain field is very sensitive. The surface length of observed cracks can be measured and their depth may be estimated from the opening displacements [20]. Full-field displacement data also allow characterization of the crack tip field, which describes the condition for crack propagation. Least-squares methods have been used to fit the Williams' series that describe the displacements or strains of a linear elastic crack to the experimental results, and so obtain the mode I stress intensity factor (SIF) [24], and this method has also been extended to mixed mode loading [25]. However, the least-squares technique is quite sensitive to accurate definition of the crack tip location [24]. An alternative approach, which is less sensitive to the crack tip position, is to use the measured displacement field as the boundary condition in a finite element analysis that calculates the potential strain energy release rate of the crack field as a contour integral (i.e. the J-integral) [26]. The analysis requires knowledge of the stress/strain behaviour of the material, and can address non–linear elastic and limited plasticity [27] and also mixed-mode loading via use of interaction integrals [28].

Elastic strains can be studied using diffraction techniques to measure interatomic planar spacings. Data may be obtained point-by-point with monochromatic X-ray diffraction (XRD), Energy-Dispersive polychromatic X-ray diffraction (EDXRD) or neutron diffraction (ND) [29–31]. Example applications include studies of fatigue crack overloads and closure [32,33], the role of residual strains in the vicinity of weld heat affected zones [34], the effect of inclusions on the strain partitioning in metal matrix composites [35] and the mechanical shielding effect of crack bridging in stress corrosion cracking [36]. Diffraction strain mapping can also be used to quantify the crack field as a stress intensity factor, and a least-square field fitting of the theoretical Williams' series to strain maps has been used to study the relationship between the SIF value and the growth rate (da/dN) for a fatigue crack [37]. Recently, the contour integral method to calculate the J-integral from a measured crack field [26] was extended by some of the authors to the analysis of diffraction data [38].

Diffraction of X-rays and neutrons has been used to study the tensile and flexural behaviour of a coarse grained polygranular graphite [10]. The study confirmed that tensile strain produced permanent deformation, whilst the behaviour under compressive loading was essentially elastic. Significantly, the applied tensile strain reduced the bulk elastic modulus and relaxed the substantial thermally induced residual elastic strains within the graphite crystals. Both of these effects were attributed to microcrack development. Microcracking is commonly observed in quasi-brittle materials, such as graphite [39] and concretes [40], and a micro-cracked fracture process zone has been observed ahead of the crack tip in nuclear graphite [15,41]. An analogy may be established between the fracture process zone and the plastic zone in ductile materials [42] as they both dissipate energy and lead to higher fracture resistance. Fracture process zones can be simulated in structural integrity calculations using cohesive models, which implement a traction-separation law, in materials such as concrete [40,43,44], graphite [45] and ceramic composites [46]. Such models are important to bridge the gap between specimen tests that provide property data, and the predictive simulation of the performance of larger engineering components.

The structural integrity assessment of nuclear graphite presents some complications, since its elastic modulus and strength increase with fast neutron irradiation [2] and decrease with radiolytic oxidation [47], but there are few data for the effects of irradiation on fracture resistance [48]. Better understanding of fracture behaviour may increase confidence in structural integrity assessments. However, if the fracture of irradiated graphite is to be understood, then non-irradiated graphite should first be addressed. Various fracture criteria for graphite have been proposed that may define a suitable cohesive model, including stress, strain and energy-based criteria [13,49]. Energy-based criteria use thermodynamic principles, whilst strain and stress criteria have the advantage of being well suited to engineering design. To determine which criterion provides the most accurate description, detailed observations of the stress and strain states in the crack tip field are required.

Three-dimensional observations of deformation and damage within materials are possible through high-resolution X-ray computed tomography (XCT) [50–53]. These can be performed with either laboratory or synchrotron facilities; the latter offers faster rates for in situ studies due to the brilliance of the X-rays. Digital volume correlation (DVC) [54] can map the relative changes in the displacement field between tomographic datasets, allowing quantitative observations of three-dimensional deformation [53,55,56]. In high quality tomographs of suitable microstructures, for which the internal features provide the necessary “speckle” contrast, the displacement measurement precision is sub-voxel,[1] and both elastic and plastic deformations may be studied. Example applications of combined tomography and image correlation include observations of granular compaction of powders [57], the measurement of elastic crack fields [58] and analysis of the deformations induced by indentation [59,60] to determine material's elastic and plastic properties by retro-engineering. Polygranular graphite is very well suited to this type of analysis, as it has significant porosity that is distributed over a wide range of length scales [2,10,15].

In this work, the progressive development of the deformation ahead of a quasi-static propagating crack in polygranular graphite is simultaneously characterised via synchrotron X-ray diffraction to measure the elastic strain field, and DVC of X-ray computed tomographs to measure the total strain field via the displacement field. The objective is to identify the fracture propagation criterion for non-irradiated graphite. This would enable more accurate simulation of fracture and damage nucleation in different specimen or component geometries. It may also guide the development of test techniques to extract the properties of irradiated nuclear graphites, which would need to be applied to small, non-standard, test specimens due to the practical difficulties of obtaining substantial specimens from operating reactors [61]. The experimental observations provide the crack's dimensions and its mode of opening under load in three-dimensions. These are implemented as boundary conditions in a finite element simulation with non-linear material properties to describe the microcracking behaviour of graphite, and the predicted stresses are verified by comparison with the experimental observations by diffraction. The calculated crack field is then used to obtain the strain energy release rate in equilibrium with the stable crack as a J-integral, which describes the criterion for mode I crack propagation.

[1] A voxel is the three-dimensional equivalent of a two-dimensional pixel.

2. Experimental details

2.1. Material

The material is one of the graphites used in the UK Advanced Gas-cooled Reactor fleet. Manufactured by Graftech (formally UCAR) and supplied by EDF Energy Generation, the moulded IM1-24 Gilsocarbon (GCMB grade) polygranular nuclear graphite has weakly anisotropic properties. Depending on orientation, the reported Young modulus, E, is between 11.6 and 11.9 GPa, with a Poisson ratio, ν, of 0.2 and a tensile strength, σ_t, between 19 and 20 MPa at a strain of approximately 2.5×10^{-3} [62]. The same grade has been studied in previous works by some of the authors [10,15,22,41]. The graphite in this work was from the same billet as the specimens of the previous study of Gilsocarbon graphite under tensile and flexural loading [10].

2.2. Specimen geometry

The test specimen (Fig. 1a) was designed to facilitate tomography and diffraction observations whilst fracture was propagated quasi-statically from a stress concentrating notch. Conventional grinding was used to prepare the specimen. Loading was applied by driving a vertical steel wedge (~10° tip angle) into the notch under displacement control. The vertical side-grooves encouraged straight crack propagation from the notch tip in a region of near-uniform thickness, and the stiffness of the specimen was increased by the greater thickness towards the outer edges.

The digitally-controlled loading rig was equipped with a 1 kN load cell (1 N precision); the balancing tensile load was taken by a polycarbonate tube (internal diameter 50 mm, external diameter 60 mm) that surrounded the specimen and was X-ray and optically transparent. Previous studies [15,41] had demonstrated the importance of wedge alignment for uniform loading of the notch, so a deep groove axial bearing allowed free rotation of the wedge around the vertical axis. The specimen was also rigidly mounted via its screw thread (M24) to a single-axis horizontal slider. The wedge was centred in the slot at the start of the experiment, with the aid of radiographs. Preparatory tests determined the typical crack initiation load and verified that straight crack propagation was reproducible over distances in excess of 5 mm, which was satisfactory for the planned experiment. For crack lengths approaching 10 mm from the notch, there was a variable tendency for the crack plane to deviate.

2.3. Synchrotron X-ray diffraction and tomography

The experiment was conducted at the Joint Engineering, Environmental and Processing (JEEP – I12) beam line at the Diamond Light Source in the UK [63]. Radiographs were recorded using a PCOedge CMOS camera (2560 × 2160 pixel, 16-bit depth), with optics selected to image an area of 8.3 × 7.0 mm (i.e. 3.24 μm per

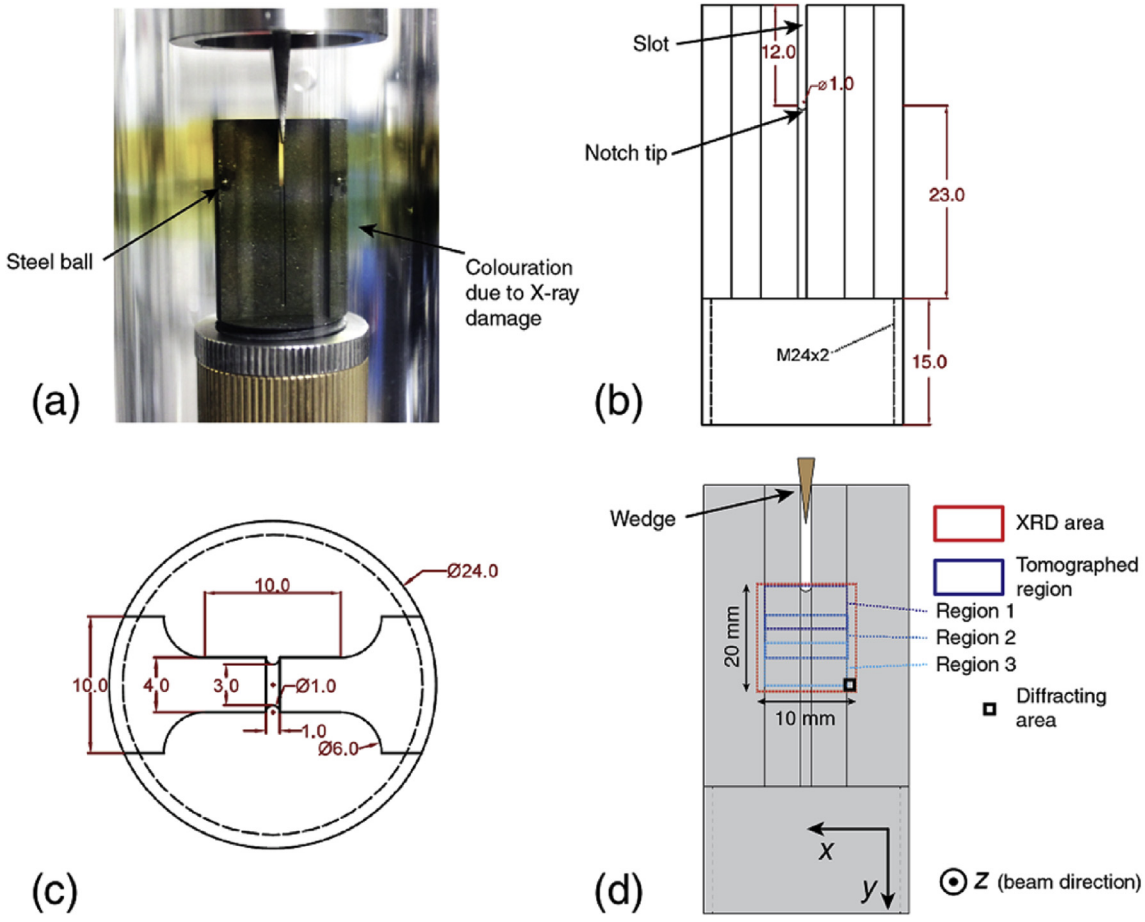

Fig. 1. (a) The specimen, with wedge inserted, showing a pair of steel balls attached as fiducial points. The specimen is within the polycarbonate tube of the loading rig, which has been discoloured by exposure to high energy X-rays (b) Side-view drawing of the specimen (c) Top view drawing of the specimen (d) Regions of diffraction maps and tomography within the specimen. The dimensions of a single diffraction measurement point ("diffracting area"), within the mapped XRD area, are shown. (A colour version of this figure can be viewed online.)

pixel). X-ray diffraction images were recorded using a Thales Pixium RF4343, 42 × 42 cm detector (2880 × 2881 pixel, 16-bit depth), located at a distance of 2.55 m from the specimen. At the chosen mono-chromatic X-ray beam energy (81.04 keV), this distance allowed the collection of Bragg diffraction rings up to a 2θ angle of about 5.5° (i.e. maximum {hkl} of {011} for graphite). Ceria powder diffraction observations were used to calibrate the detector distance from the vertical rotation axis of the specimen stage. Slits were used to reduce the incident X-ray beam to a size of 1.5 × 1.5 mm for the diffraction observations. They were removed for radiography and tomography. The exposures were 1 s for each diffraction pattern and 0.3 s for radiographs.

Tomographs were recorded with 3000 radiographs over a 180° rotation, and a standard back-filtered projection algorithm [64] was used for the image reconstructions. For noise reduction, a slice-by-slice 2-D median filter of 1 pixel radius was applied to the horizontal slices of the reconstructed 3-D volumes using the software ImageJ [65]. At each observation, three overlapping tomographs were acquired to record a total volume of 17.0 × 7.0 × 7.0 mm, the overlap between tomographs was 2 mm in the vertical axis (Fig. 1d). The maximum path length of X-rays through the specimen was greater than the dimension of the tomographed volume, but due to the low X-ray attenuation of graphite, no corrections for the specimen geometry were applied in the reconstruction of these region-of-interest tomographs.

The diffraction maps were collected in the *x*-*y* plane, with the beam oriented in the *z*-direction (Fig. 1d). The measurement points were positioned at 750 μm intervals, by translation of the specimen, to map a rectangular region measuring 20 mm in the *y* direction and 10 mm in the *x* direction. Each diffracting gauge volume had a 50% overlap at the incident surface with adjacent measurements. The mapped region was centred horizontally on the notch tip, and positioned vertically to include the notch tip and the region beyond. Radiographs of the specimen with small fiducial steel balls attached to its surface were used to align the notch parallel to the beam.

Computer scripts were used to control the experiment, in particular automating the detector and specimen movements for the changeover between imaging and diffraction modes, the diffraction mapping and the collection of consecutive overlapping tomographs. A synchrotron X-ray beam interruption occurred near to the end of the allocation period of the experiment, and one diffraction map was acquired during a transient of the X-ray monochromator temperature. This slightly affected the beam energy, and these data were corrected using the procedure described in the Supporting information, Section 1.

2.4. Loading sequence

A reference tomograph and a reference diffraction map were obtained with the wedge inserted at a pre-load of 8 N. The wedge was then inserted further in displacement control at a rate of 0.2 mm/min whilst the load was monitored. Visual inspection of radiographs was used to assess the approximate increment of the crack length, and the wedge insertion was arrested at constant displacement when the crack was judged to have propagated a sufficient distance. A set of tomographs and a diffraction map were obtained of the loaded specimen, which was then unloaded completely by removal of the wedge, and tomography and diffraction mapping were repeated. This procedure was cycled to obtain 5 sets of loaded and unloaded data of a progressively propagated crack, although the available beam time did not permit the collection of a final set of tomographs of the unloaded specimen in the 5th cycle.

3. Analysis methods

3.1. X-ray tomography and digital volume correlation

Image thresholding and segmentation methods that are commonly used to quantify the dimensions of cracks in X-ray tomographs are difficult to apply in nuclear graphite due to the high levels of connected porosity [15]. Hence, the tomographs of the loaded specimen were visually inspected, slice-by-slice, to identify the crack tip position at intervals of 50 pixels (~160 μm) across the specimen thickness. The uncertainty in the assessment of crack tip position at each point was conservatively estimated to be 32 μm (i.e. 10 pixels).

DVC analysis was applied to all of the tomographs to retrieve the displacement field relative to the reference tomograph. The 16-bit images were first converted to 8-bit; the extreme values of the 8-bit range (i.e. 0 and 255) were assigned to the same minimum and maximum grey level values that were observed in the 16-bit data for all the scans, with the objective of reducing the potential data loss in this process. Each tomograph was cropped to 2560 × 1536 x 2112 voxels to remove the majority of the empty volume outside of the specimen. The DVC analysis was performed using the LaVision DaVis (Version 8.1) software, employing a multipass FFT-based algorithm; the first pass used cubic subset sizes of 256^3 voxels with an overlap between subsets of 75% and the second pass 128^3 voxels with 75% overlap. All points with a correlation coefficient below 0.8 were discarded (i.e. set to NaN values). For each observation, the 3 overlapping tomographs were processed separately and the displacement vector data were stitched by averaging in the overlapped region. On comparison of the average vector representative of each tomograph in the overlap region, the magnitude of the difference between vectors was less than 2.0 μm (i.e. 0.6 voxel). This was regarded as a measure of the uncertainty in the DVC measurement of displacements. The combined dataset was then corrected for small rigid body displacements and rigid body rotations, measured relative to the reference, based on the algorithm described in Ref. [59]. The final data have a coordinate system defined such that: the lowest point of the notch tip is at $y = 0$ and the y axis is positive towards the bottom of the specimen; the x axis is positive towards the right, with the notch tip at $x = 4.5$ mm; and the z axis is in the X-ray beam propagation direction, with centre of the notch at $z = 1.5$ mm.

3.2. Strain mapping by diffraction

The raw diffraction data are images of the Bragg diffraction rings, containing all reflections to a maximum Bragg angle of ~5.5°. An example X-ray diffraction pattern is shown in Fig. 2. A large slit size of 1.5 mm was chosen as the diffraction patterns from smaller slits can be affected by local texture in the coarse Gilsocarbon microstructure [2,66]. The (002) ring located at 2.55° was of interest as it has the highest intensity and the anisotropic graphite crystal has its largest elastic compliance normal to this plane; the effect of tensile loading on this reflection has been studied previously by some of the authors [10] using a cross-correlation methodology to measure diffraction peak shifts with improved precision. Ring centres were determined by ellipse fitting of a cerium oxide (CeO2) power calibration sample, and then data averaging was done by binning at 1° intervals of azimuth angle, so that for each sector a radial intensity profile was obtained by integration. For additional details on peak shape in similar experiments, the reader may refer to [10], which compares X-ray and neutron diffraction. The cross-correlation method was applied to measure the shift of the (002) peak (i.e. the change in ring radius) relative to the reference diffraction data at the same position on the

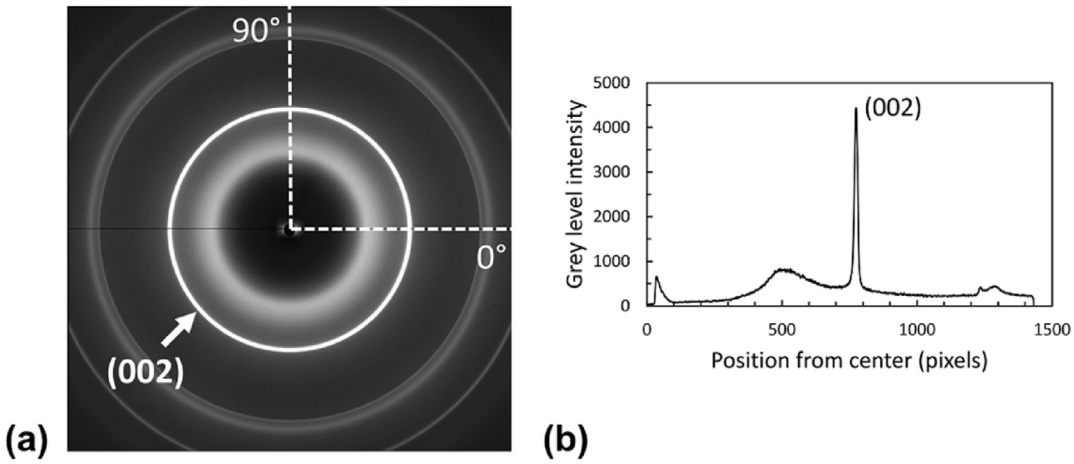

Fig. 2. Example X-ray diffraction image for Gilsocarbon graphite, with a line profile of the measured intensity (16 bit) along the radius at 0° at a sample to detector distance of 2.55 m. The (002) Bragg reflection is marked. The pixel size is 148 μm.

specimen, so retrieving the principal strains and their azimuth orientation. A rotation matrix was applied to the principal strain diagonal tensor to retrieve the strains ε_{xx}, ε_{yy} and ε_{xy} in the coordinate system of the specimen. This was done for all of the 378 diffraction patterns that constituted each diffraction map, and the data were visualised using contour plot methods in Matlab®. Strains calculated by this analysis method in polygranular graphite have a random measurement error of 1.2×10^{-5} [10].

Applied loads may cause movements of the specimen along the direction of the beam that will have a geometric magnifying or diminutive effect on the diffraction ring radius [10], which introduces artificial strains. The experimental set-up did not permit calibration of the specimen to detector distance (e.g. with a ceria reference) once loading has commenced, so the effects of specimen movements were corrected for each diffraction data point by direct measurement of the specimen position, relative to the calibrated rotation axis, using the raw tomography/DVC results. These had not been corrected for rigid body movements, and so measured the specimen position in the frame of reference of the synchrotron. The displacements along the beam were determined by first averaging the DVC-measured displacements through the specimen thickness in the beam direction. These had a spatial interval of ~100 μm, so the obtained 2-D displacement field was interpolated to obtain the displacement at the exact position of each diffraction measurement. In the previous study of a tensile test of graphite [10], the corrections for specimen movement were quite significant due to the flexibility of the load train, but in this case, due to the high rigidity of the loading jig, the maximum movement was between 6 and 10 μm in the *z* direction and did not change significantly with applied load. Without correction, this movement would introduce a strain bias of approximately 4×10^{-6}. There is no measurable error from the positioning reproducibility of the Pixium detector between diffraction observations; this was measured using image correlation of diffraction images to be better than 1 μm.

4. Results

The raw data of the load vs. crosshead displacement for the 5 load cycles are presented in Fig. 3, in which the red crosses identify the recording of diffraction maps and tomographs whilst the specimen was maintained under load at a fixed wedge displacement. The load at these observations was manually recorded, before and after each mapping and imaging sequence, and did not reduce by more than 12% over each period. Contact between the

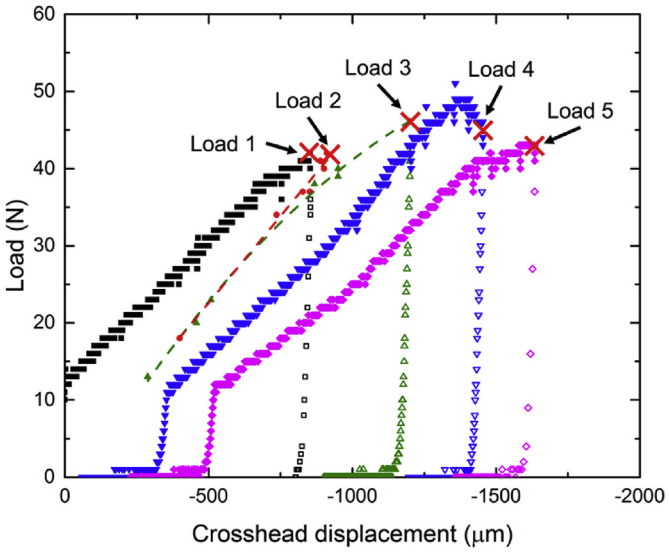

Fig. 3. Load – crosshead displacement data for all cycles; loading is shown with solid symbols, and unloading with open symbols. For Cycle 2 and Cycle 3, the loading curve is traced through the available data using a quadratic best-fit (both $R^2 > 0.99$). Tomographs and diffraction maps were collected at the points labelled "Load 1" etc. (A colour version of this figure can be viewed online.)

wedge and the test specimen above 10 N is apparent in the initial loading of each cycle – the wedge was removed completely between each cycle. The data are offset in displacement between cycles, which is attributed to damage that occurred at the contact between the wedge and the specimen. The reported displacements do not correctly represent the wedge position in the specimen's notch during unloading. This is due to friction that allowed slack movement in the thrust bearing to be taken up when the crosshead displacement was reversed, before the wedge itself was removed. A software issue affected data logging during cycles 2 and 3 and fewer load/displacement data points are available to show the loading curves, so the trend line has been fitted through the available data.

The radiographs (e.g. Fig. 4), were adequate to assess the approximate position of the crack tip during the experiment, but are not sufficiently sensitive for reliable measurements of the crack dimensions. This was done using the tomography data. Example sections of a tomograph of the specimen (cycle 3, loaded) are presented in Fig. 5. Automatic segmentation of the crack is

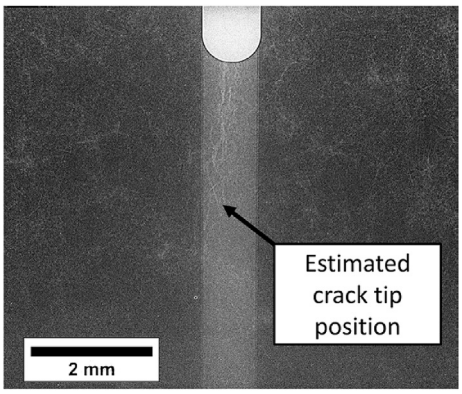

Fig. 4. Radiograph taken at Cycle 3 (Loaded), used for approximate monitoring of crack length during the experiment.

unreliable due to the high density of connected pores, so a manual slice-by-slice segmentation was done to provide a 3-D visualization of the crack. This confirms a straight crack has propagated parallel to the notch plane. The crack is continuous, with some bridged regions apparent as holes in the crack [18]. Some of the bridges near to the crack tip may be positions where the crack opening displacement is too small, compared to the voxel size, to provide sufficient contrast [22].

The crack's geometry was also measured using a 3-D edge detection analysis (E-D) that employs a method [67] based on phase congruency. Applied to the displacement field, it is very sensitive to the discontinuity of the crack. The positional uncertainty depends on the interval between displacement vectors, which in this case is 100 μm. The crack opening displacements were obtained from the difference between the closest DVC displacement vectors on either side of the crack, with an uncertainty that depends on the DVC measurement precision (i.e. ~2 μm). Applied to the DVC data (Fig. 6a), this provides a direct 2-D measurement of the crack opening profile over the crack plane (Fig. 6b), and shows that the crack does not fully close when the load is removed. The crack length was measured using both the visual analysis of the tomographs (loaded) and the edge detection analysis of the displacement field (loaded and unloaded). Measurements were made of the crack depth from the notch across the specimen thickness (Fig. 7a); the standard deviation of the observations provides the uncertainty in crack tip position, which was around 0.4 mm for both types of analysis. A good agreement is observed between the two methods for the loaded crack, but the edge-detection analysis of the unloaded displacements consistently shows a shorter crack length than the loaded data.

The observations of the loaded crack define its shape (Fig. 7b). Crack initiation occurred in cycle 1, which is also indicated by the reduction in the load/displacement gradient observed above 40 N (Fig. 3), but the crack did not propagate fully across the specimen thickness; in this cycle the maximum deviation of the observed crack front from the average crack length (including the notch

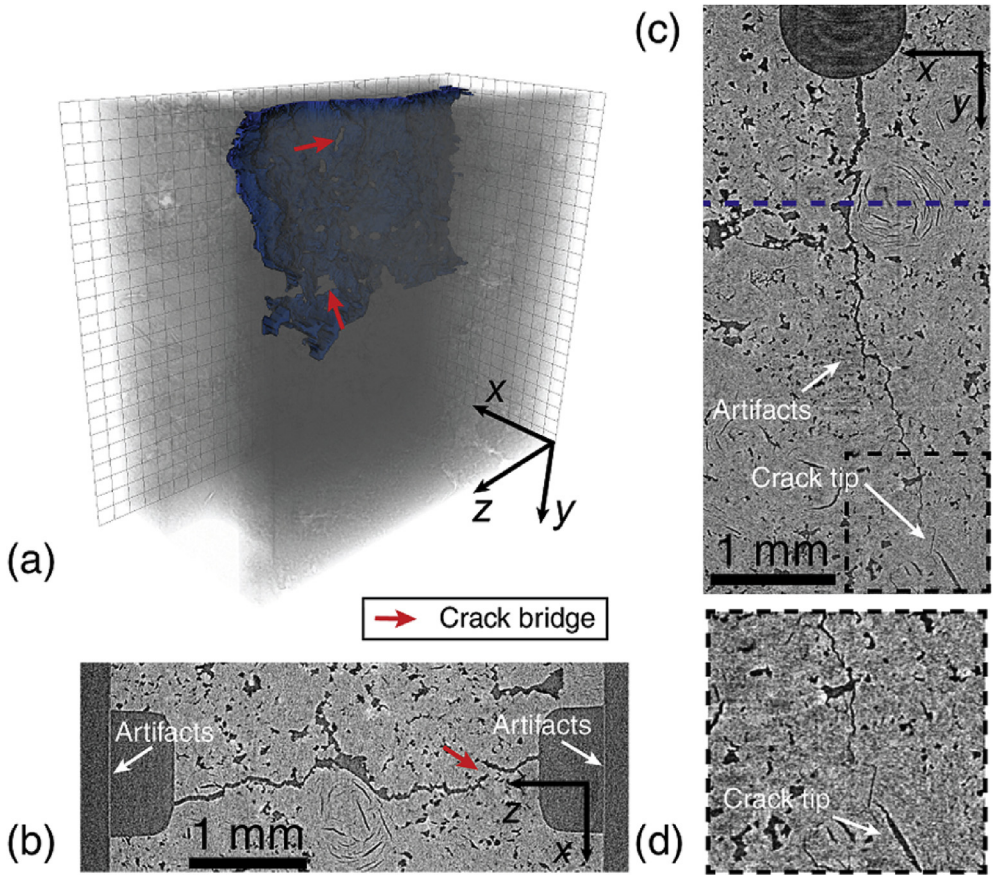

Fig. 5. The crack at Cycle 3, loaded. (a) 3-D visualization of the manual segmentation of the crack (each square on the grid is 320 μm); (b) xz-planar slice (c) yx-planar slice; The position of slice in (b) is shown as a dotted line in (c). Artefacts due to the 'region of interest' tomography can be seen in the central section of (c), close to the rotation axis, and also at the mouths of the side-grooves in (b); (d) zoomed view of the crack tip region, which is outlined by a dashed box in (c). Some crack bridges are indicated in by arrows in (a) and (b). (A colour version of this figure can be viewed online.)

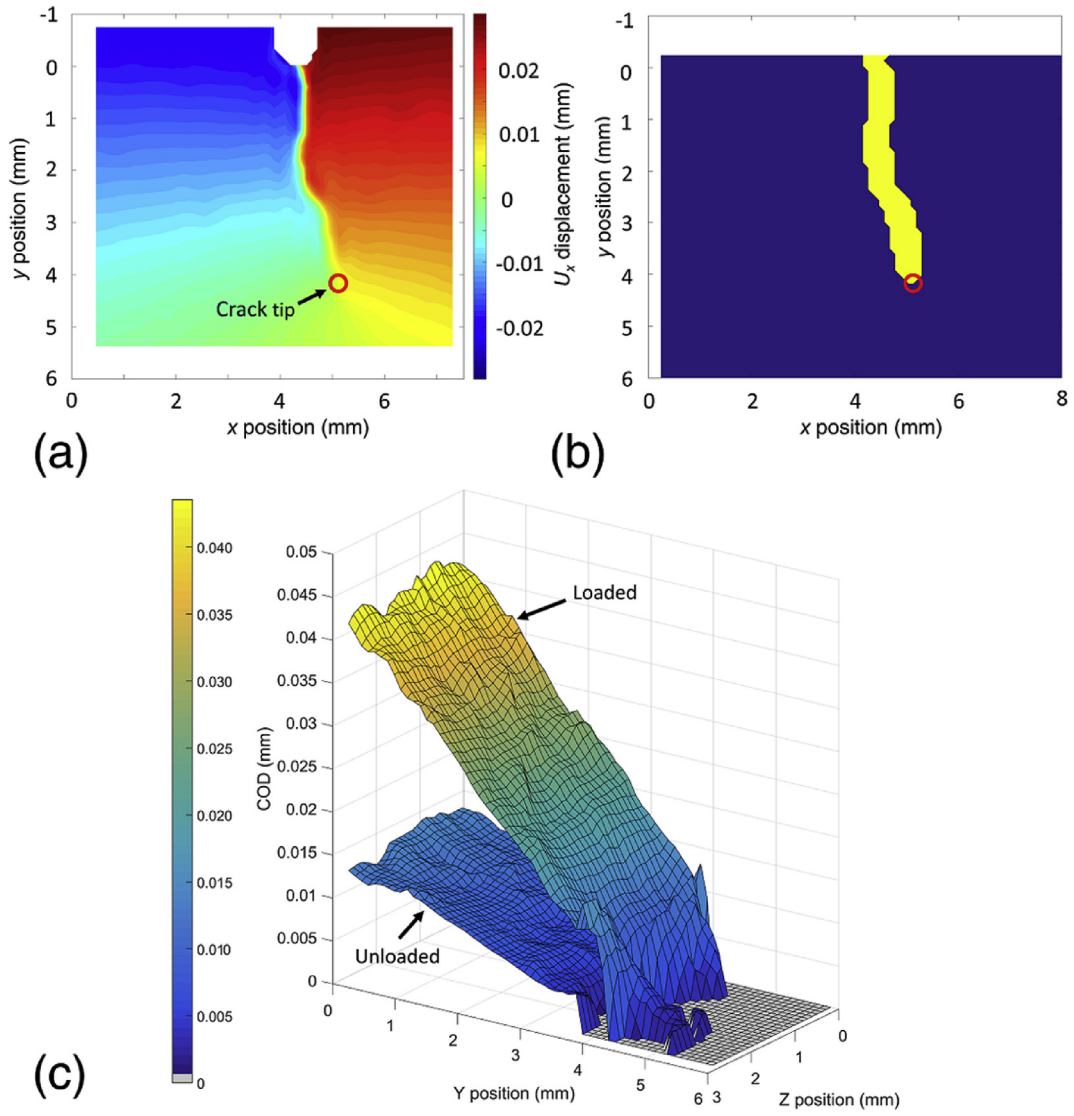

Fig. 6. (a) Example map of the Ux displacement field obtained by DVC of tomographs (Cycle 3, loaded), shown in the xy plane at z = 1.5 mm, compared with (b) edge-detection (E–D) applied to the same displacement field by phase-congruency, the technique produces a binary image; pixels detected as part of an edge (i.e. crack) are shown in yellow. The crack tip position, detected by E-D, is shown as a red circle; (c) 3-D measurement of the crack opening displacements for Cycle 3 (Loaded and Unloaded) using the E-D method. The notch tip is at y = 0. (A colour version of this figure can be viewed online.)

depth) was ~8%, measured using edge detection. There was no significant propagation of the crack front in the second cycle. This is consistent with the linear load/displacement trace measured during loading in cycle 2, although in this cycle the crack developed fully across the specimen thickness to achieve a more uniform crack length. The load peak in cycle 4 and the load plateau in cycle 5 indicate further crack extension, which is confirmed by the tomographs, and although the load/displacement data in cycle 3 are sparse, there is a clear decrease in the load/displacement gradient above 40 N that is consistent with crack propagation. In cycles 2 to 5, the maximum deviation of the crack front from the average crack length, measured by edge detection, was ~5%, (average 1.7%). The visual analysis of the tomographs shows that the crack was always within 0.4 mm of the central plane of the specimen, except for cycle 5 where the crack deviated by up to 1 mm at some positions. In all cycles, the maximum deviation of the crack plane was less than 17°, measured over an arbitrary distance of 2 mm from the crack tip, thus in terms of the closest relevant standard (e.g. ASTM 647 [68]) the crack was essentially planar.

Two different analysis methods were used to assess the mode I crack openings (Fig. 8). The first (DVC) had been applied in previous studies [41] and measures the difference between the U_x displacements on either side of the crack in the direction perpendicular to the notch plane. These were obtained at a fixed position of $z = 1.5$ mm that is close to the specimen's central axis, along two 0.4 mm wide bands running in the x direction that are located at approximately 0.4 mm on either side of the crack. The distance between each DVC data point is ~0.1 mm, so 4 points were averaged at each y position. Data points where the standard deviation of the displacement vector magnitude of the averaged points was higher than their average value were censored. The censored points are less than 1% of the data and arise from poor DVC correlation; they were preferentially located at the bottom of the tomographs (probably due to the shape of the X-ray beam) and therefore affected regions where the tomographs overlapped (shown in light grey in Fig. 8a and b). Censored points also arise from local effects of ring artefacts in the tomographs. Ring artefacts are caused by defects in the optical imaging system, such as dust on the scintillator,

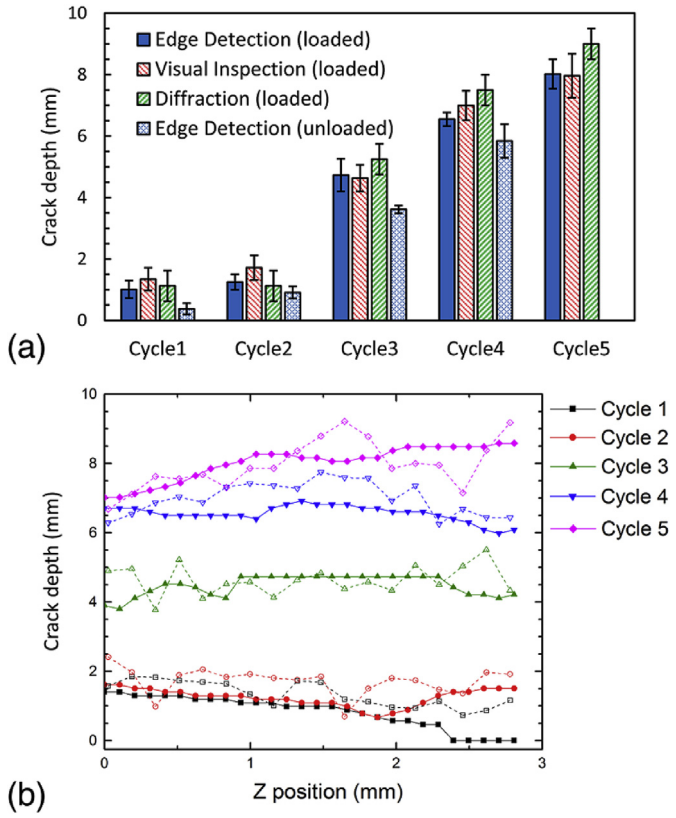

Fig. 7. Measurement of the crack length: (a) Average crack depths (measured from notch tip at y = 0 mm), obtained by assessment of the crack tip position by visual inspection of tomographs and edge-detection analysis of the DVC displacement field. The crack tip position, assessed from the location of the strain peak measured by diffraction, is also shown; (b) Crack depth across the specimen thickness, measured under load – the full symbols show data obtained by edge-detection analysis (measurement error ~100 μm) of the DVC displacement field, open symbols show data obtained by visual inspection of tomographs (measurement error ~30 μm). (A colour version of this figure can be viewed online.)

the optics and/or the detector or faulty pixels on the sensor. This generates artefacts at a fixed position on the radiographs that become rings in the reconstructed image and influence the DVC measured strains [64].

The second method (E-D) used the edge-detection method to identify the discontinuity of the crack [67]; the crack opening displacement was obtained as the relative displacement between the displacement vectors closest to the discontinuity, so no data were extracted ahead of the crack tip. Here also, the position $z = 1.5$ mm was considered. Both crack opening profiles are quite similar, as shown by the examples in Fig. 8a and b, and both show the residual opening of the crack after unloading that is visualised in Fig. 6b. The crack tip position is sharply defined by the edge-detection method, but the DVC analysis shows a significant zone ahead of the loaded crack tip, several mm in length, with a measurable displacement difference across the crack plane. Observed previously [15], this has been attributed to the effect of microcracking in the fracture process zone. It is not found by the edge detection method, which is sensitive to steeper gradients in the displacement field. The full field analysis of tomographs provides 3-D vector displacement data, so the relative displacements that create mode II and mode III shearing of the crack faces can also be examined. Measurements were extracted using the edge-detection analysis, at the crack mouth (i.e. at $y = 0$) at all z positions and were averaged (Fig. 8c). The mode I displacement at this position increases with crack length. There is no significant mode II displacement in any observation, nor is there a significant mode III displacement until the final observation at the longest crack length. Hence the crack is loaded in mode I, except for the final observation (cycle 5), which has mixed mode loading.

The elastic strains ε_{xx}, ε_{yy} and ε_{xy}, measured by diffraction mapping of the change in the (002) interplanar spacing, are presented in Fig. 9 for both the loaded and unloaded states for each of the loading cycles. In the loaded state, there is a tensile peak in the strain field ahead of the notch that moves further from the notch with successive load cycles. When unloaded, a region of compressive strain extends to approximately the same position. This is shown in more detail in Fig. 10, using the strain ε_{xx}. The data are the average, at the same distance, of the elastic strains in a band of 3 mm thickness that is parallel to the notch plane; this band is identified in Fig. 10 (see ε_{xx}. unloaded, cycle 1). The strains are presented as a function of distance from the crack tip, identified by the visual examination of the tomographs at that location (i.e. Fig. 7), for which the positional uncertainty is approximately 30 μm. The peak strain is, on average, located at the crack tip position and there is a gradual increase in strain from cycles 1 to 5. There are tensile strains behind the crack tip when it is loaded, over a distance that increases to 5 mm as the crack propagates, and these strains become generally compressive when the load is removed.

5. Analysis

The crack is approximately planar with a reasonably straight crack front (Fig. 7b) and it is loaded predominantly in mode I (Fig. 8c), except for the final observation at the longest length that has a significant component of mode III shear. The average crack tip position is identified similarly by both visualization and measurement of the crack opening displacements; the average difference between the two techniques is of 220 μm, with the visual measurement being consistently equal or longer than the measurement from the crack opening displacements (Fig. 7a). So the crack is visualised well by X-ray tomography at 3.24 μm voxel resolution. The crack opening displacement data show the crack remains open when unloaded, with an opening that is approximately 20–30% of the crack opening displacement of the previous loading step (Fig. 8). This is consistent with previous measurements [15], and may be attributed to the fracture surface roughness that prevents full closure of the crack.

The fracture process zone is apparent as a zone of increased displacement ahead of the loaded crack tip (Fig. 8), which is shown by the difference between the edge-detection and the direct DVC measurements. The XRD maps in the unloaded state show significant compressive strains in the crack wake (Figs. 9 and 10a). The previous diffraction study of tensile loading in graphite [10] also found a compressive strain change relative to the as-received condition after the application of small tensile strains. This was proposed to be the result of relaxation, via microcracking, of the significant thermal residual stresses that exist in the microstructure after cooling from the high temperature graphitisation treatment. The observation of a compressive strain change in the crack wake is further evidence of a fracture process zone that is damaged by tensile strain. Its size remains approximately 2 mm as the crack extends. The tensile strain profiles (Fig. 10b) for cycles 2 and 3 exhibit the classical inverse square root singularity of an elastic crack field, although this cannot be affirmed for cycle 1, 4 and 5. This may be due to the non-linear deformation and micro-cracking damage in the fracture process zone, which could affect the shape of the elastic crack field.

The objective of this work is to determine the fracture criterion for graphite. As the observations of the loaded crack were obtained in static equilibrium with the applied deformation that caused it to

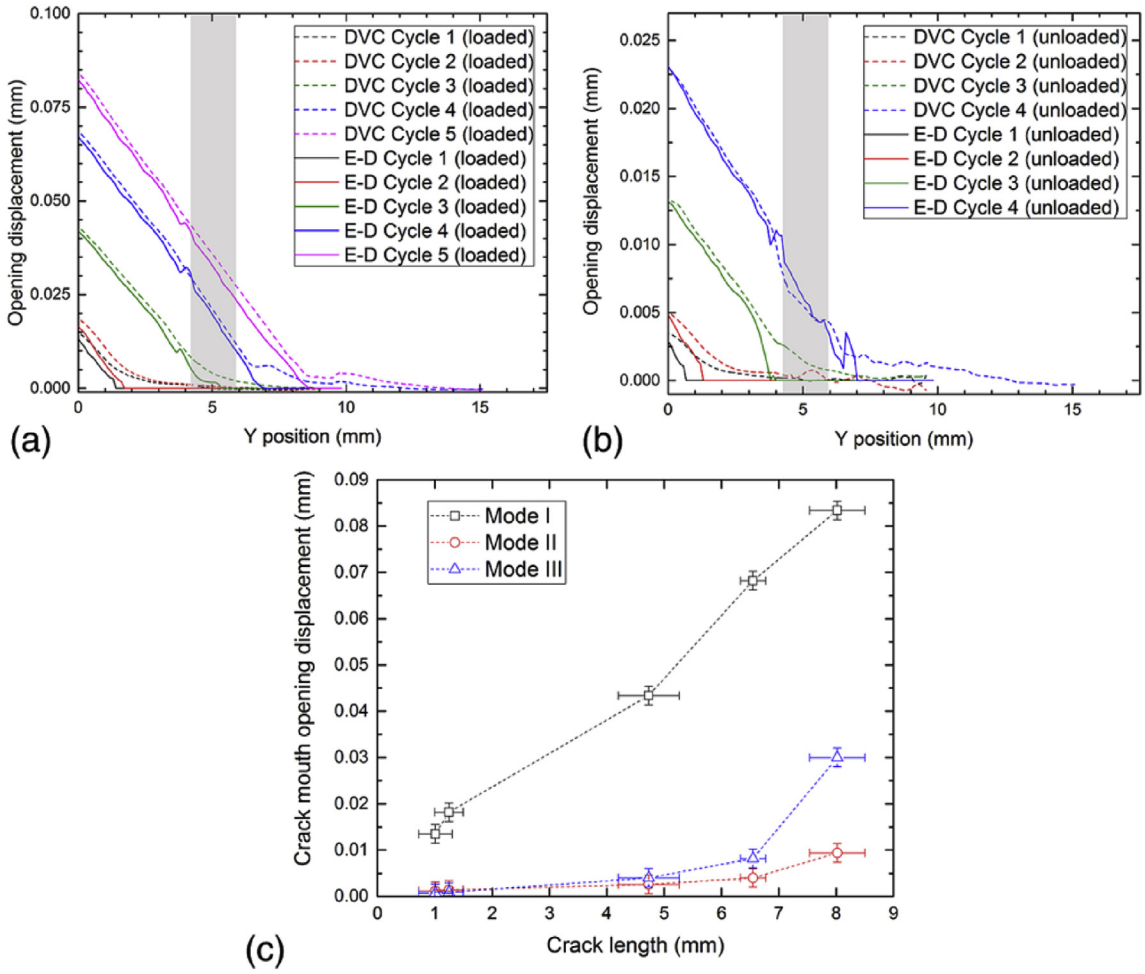

Fig. 8. Measurements of the crack opening displacements. The mode I opening profile was obtained by both direct DVC analysis and edge detection (E–D) processing of the displacement field. The data are recorded at the centreline position, (z = 1.5 mm) in the (a) loaded and (b) unloaded states (the region where tomographs overlap is indicated in light grey). In (c) the mode I, mode II and mode III crack mouth displacements are shown for the loaded state; the data are taken at the notch position (i.e. y = 0 mm) averaged along the z direction. (A colour version of this figure can be viewed online.)

propagate, it is assumed that the states of stress and strain ahead of the crack tip are representative of this criterion. The simplest fracture propagation criterion would be a critical strain or stress [8,69,70], which might be assessed at some characteristic distance from the crack tip. The magnitude of the total strain in the fracture process zone can be estimated using the mode I displacement difference, measured by DVC across the crack plane at an arbitrary distance of 0.5 mm ahead of the crack tip (Fig. 11). This displacement difference has no significant trend with crack length, and it has an average value of 7.4 μm: measured over a gauge length of 0.8 mm, this represents an approximate strain of 9.25×10^{-3}. This might support a total strain criterion. However, the diffraction-measured elastic strains ahead of the crack tip increase in magnitude with crack extension (i.e. the peak strains in Fig. 10), which suggests that a constant strain failure criterion is insufficient. A best fit to the relationship between applied stress and the elastic strain measured by diffraction, obtained in a tensile test [10] (see Supporting information, Section 3), was used to estimate the stress at the strain peak (Fig. 11). Both the elastic strain and stress increase as the crack extends, so a constant stress failure criterion is also insufficient to describe the condition for crack propagation.

The crack field governs the rate of release of elastic strain energy that is available for crack extension. It is necessary condition for crack propagation that this exceeds the energy required to extend the crack by surface creation and associated non-reversible damage mechanisms. The elastic strain energy release rate of the strain field of a crack is described by its J-integral [71]. Commonly used in structural integrity assessments of cracked components, the J-integral can be obtained directly by finite element simulation with knowledge of the applied loading, component geometry and material properties. The J-integral in static equilibrium with a loaded crack can also be calculated from experimental observations of the displacement or strain field [26,55]. The displacement field data obtained in this work were therefore analysed to calculate the J-integral in the loaded specimen as the crack was quasi-statically extended, to investigate whether this described the necessary fracture criteria. The analysis method, which injects the displacement field into a Finite Element (FE) simulation as the boundary conditions, has an advantage over field fitting approaches (e.g. Ref. [56]), as it does not need to assume that the crack field follows a particular function, such as the singularity of a stress concentration in a linear elastic material. This is of particular utility for quasi-brittle materials such as graphite, which exhibits a non-linear stress-strain relationship and a change in elastic modulus with tensile strain [10]. The original method [72] used a 2-D model to analyse surface DIC data. It has been extended here to three dimensions to make use of the volumetric data provided by DVC, as detailed in the Supporting information, Section 2. A description of

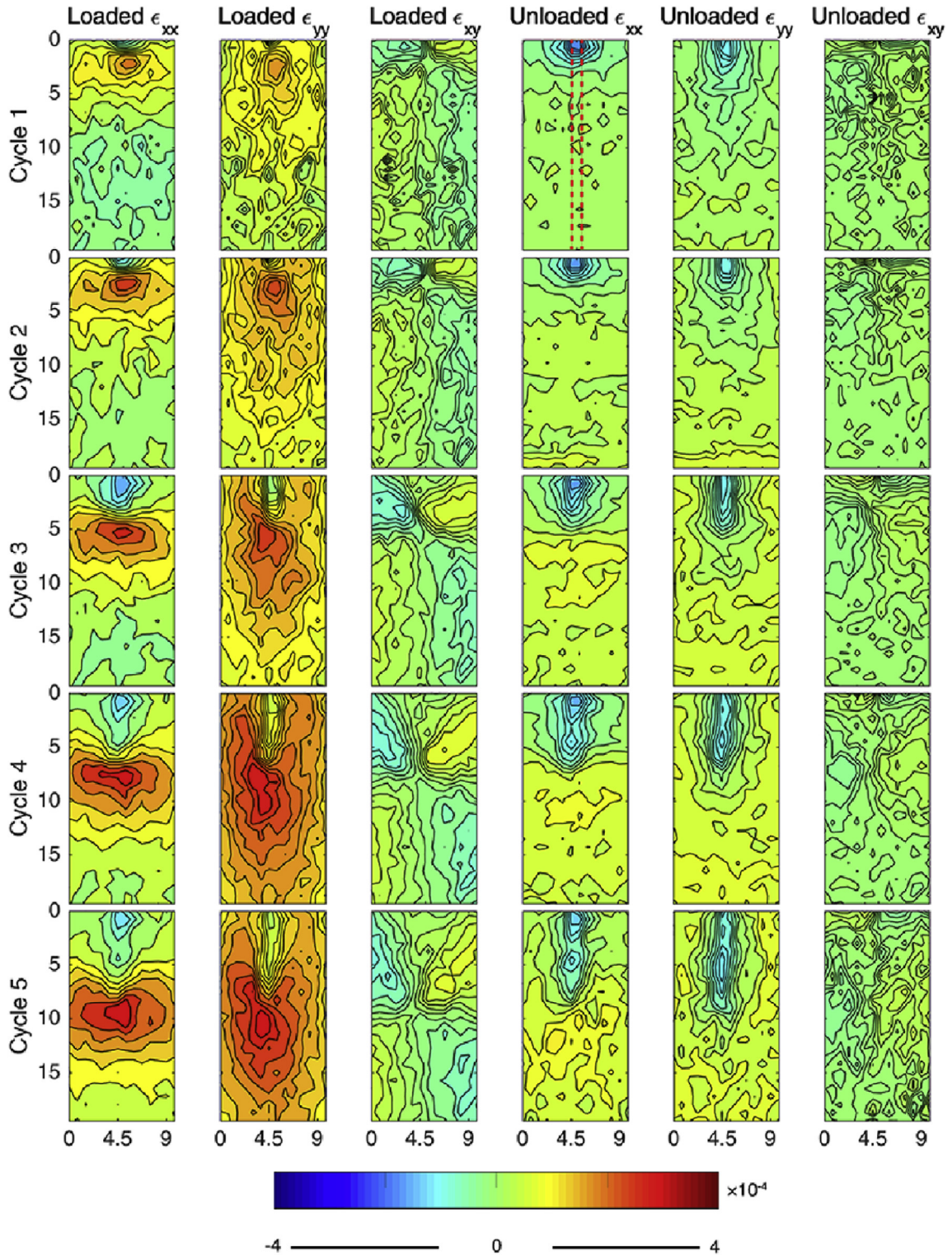

Fig. 9. Diffraction maps for all load and unload states. The region used for the strain profiles that are presented in Fig. 10 is defined on Cycle1, Unloaded (ε_{xx}). (A colour version of this figure can be viewed online.)

its application is provided here.

Three-dimensional FE models (in Abaqus 6.13) of the crack were meshed with eight-node linear brick elements that used full integration (i.e. 8 integration points per element). The element mesh size was 45 μm in the crack tip region, increasing to 250 μm at positions remote from the crack tip to reduce computational cost. Each FE model was registered in position and orientation with the reference tomograph, and so was also registered with the displacement field provided by the DVC analysis. A planar crack was defined with constant length across the specimen thickness, using the average crack lengths measured by the visual observation of the tomographs. A full model of the test specimen was not required in

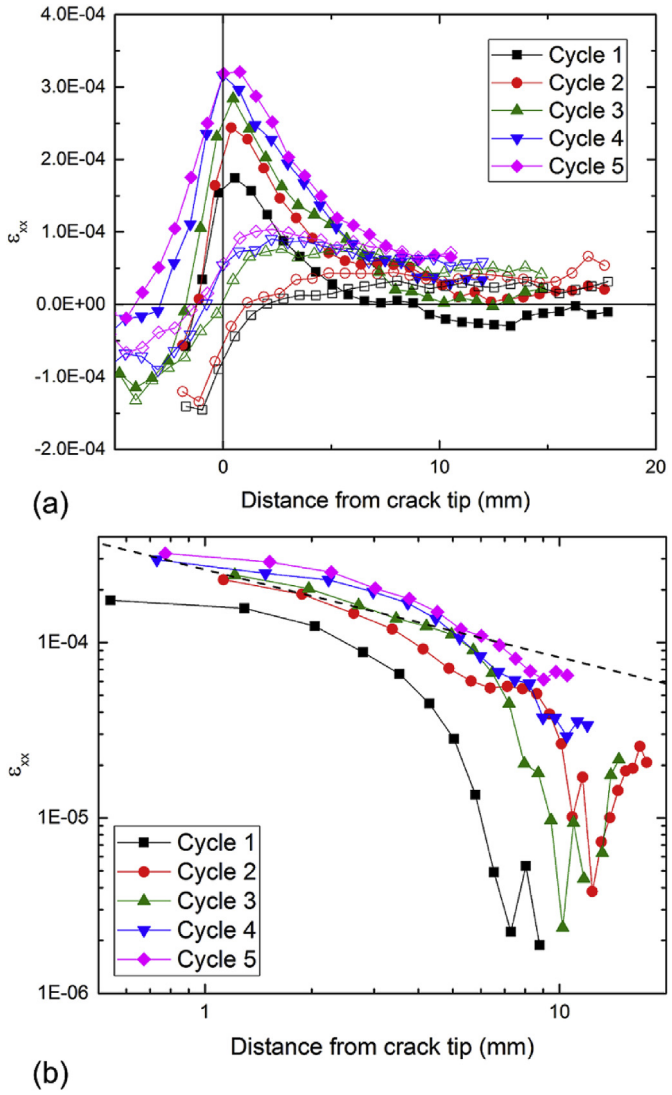

Fig. 10. Elastic strain profiles measured by diffraction, presented as ε_{xx}, as a function of distance from the crack tip. Data for the loaded state are shown in full symbols, and the unloaded state in open symbols. The crack tip position was determined from the visual observation of tomographs. The expected uncertainty in strain measurement is 1.2×10^{-5}. (a) linear axis scale (b) log-log axis scale (loaded data ahead of the crack tip only, for clarity). The dashed line shows the gradient of the theoretical linear elastic singularity ($1/r^{0.5}$). (A colour version of this figure can be viewed online.)

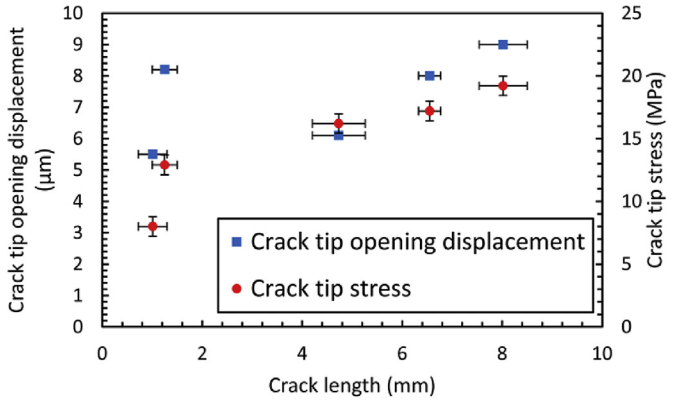

Fig. 11. The crack tip opening displacement, measured by DVC at a distance of 0.5 mm ahead of the visually observed crack tip, as a function of the average crack length. The crack tip stress (i.e. the peak stress ahead of the crack tip), σ_{xx}, measured perpendicular to the crack plane is calculated from the XRD determined peak strain, ε_{xx}, using the empirical relationship measured in Ref. [10] (reproduced in Supporting information, Section 3). (A colour version of this figure can be viewed online.)

this analysis, and the model has the same dimensions as the DVC data (a figure of the model is shown in the Supporting information, Section 2), which are on a regular 3-D grid of 96 μm intervals (32^3 voxels). This does not match the FE mesh, so the DVC data were interpolated onto the FE mesh using a Radial Basis Function (RBF) network interpolator, based on the techniques described in Ref. [73] and coded in Matlab®. The DVC data were censored (i.e. masked) close to the crack tip where DVC may give erroneous results due to steep strain gradients and the discontinuity of the crack [74]; the mask was applied to a volume of 1.5 mm width, centred on the notch and extending 3 mm beyond the crack tip (the arrangement of the mask is presented in the Supporting information, Section 2). The FE model calculates the displacements within the masked region, since the displacements of the nodes at its boundary are provided by the DVC measurements. The J-integral integration contours are within the masked region, as the noise in the DVC data did not allow reliable calculation of a contour-independent J-integral from the directly measured displacements. No experimental data from the fracture process zone were used, as it was within the masked region. The J-integral was calculated over 20 contours to verify contour independency and the volume integral approach natively implemented in Abaqus was used [75]. This provided a J-integral evaluation at all the nodes along the crack front. These were averaged, and the standard deviation, which was greater than the variation between contours, was used as a measure of the uncertainty of the J-integral. The analysis makes no use of the applied load-displacement data (i.e. Fig. 3). Due to the computationally intensive aspect of the problem, each FE model was run on a high-end workstation using CPU parallelization over 8 cores.

The J-integral calculations were performed for the displacement fields obtained in the loaded condition of each cycle. Two material models were implemented: (i) an isotropic linear elastic model with typical bulk properties of Gilsocarbon graphite [62] ($E = 11600$ MPa, $\nu = 0.20$); and (ii) an isotropic non-linear elastic model described with a custom UMAT (User-defined MATerial law) coded in Fortran, which determines the element's elastic modulus as a function of the maximal principal tensile strain in the element. The calibration for the UMAT is provided in the Supporting information, Section 3. The Young's modulus is not affected by compressive loading and a numerical limit was imposed for tensile strains above 1% in order to prevent numerical instability. Such high strains occurred only in crack tip elements.

The results were assessed by comparison of the σ_{xx} stress profiles calculated by FE with stresses calculated from the diffraction measured strains (ε_{xx}) (Fig. 10) using the tensile strain-stress calibration curve obtained in Ref. [10] (reproduced in Supporting information, Section 3). Due to the diffraction slit size, each XRD data point represents the average stresses in a region measuring 1.5×1.5 mm, projected through the specimen thickness. To allow a direct comparison, the FE data were binned over a 1.5 mm gauge length with a moving average (Fig. 12a), which has the effect of reducing the maximum stress reported close to the crack tip. Assumption of linear elasticity significantly increases the stresses, even with binning, whereas the non-linear UMAT provides a generally good agreement with the experimental data for all the load cycles (Fig. 12b), particularly at high stress. The poor agreement at lower stresses in cycle 4 may be due to DVC errors arising from ring artefacts in the tomography data for this cycle.

The J-integral was calculated from the FE simulations, using

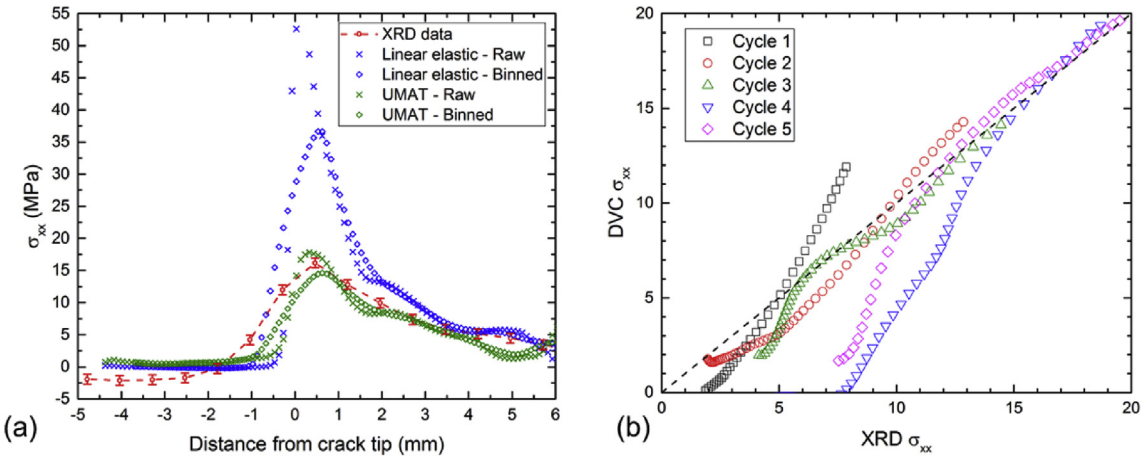

Fig. 12. (a) Stress profiles (σ_{xx}) perpendicular to the crack plane for cycle 3 (Loaded), presenting a comparison between the XRD data and FE data with constant and UMAT-defined elastic properties. The positions of the XRD data are measured relative to the crack tip position defined by the visual observations of the tomographs. The 'raw' data is binned in the x direction over 1.5 mm, this has little effect on the data; The 'binned' data has an additional binning applied on the y axis, it reproduces the averaging effect of the XRD slit size. (b) A 1-to-1 comparison between the XRD and FE stress data for all points with a distance ahead of the crack tip. Error in the stresses is estimated around ±0.8 MPa. (A colour version of this figure can be viewed online.)

both a constant elastic modulus and the UMAT properties (Fig. 13). Higher values are obtained with constant elastic modulus due to the higher stresses close to the crack tip compared to the UMAT, which reduces the elastic modulus with increasing tensile strain. The results from the first cycle (Load 1) are unlikely to be valid as the curved crack front (i.e. Fig. 7b) would reduce the deformation measured by DVC, and so reduce the calculated strain energy. The ring artefacts that influence the total strains in cycle 4 affect only the lower stressed regions (Fig. 12b), and so do not significantly affect the J-integral calculation. For the last cycle (Load 5), the shear strains from the significant Mode III loading add to the J-integral, which does not separate the strain energy contributions of the different modes. To calculate the mode I strain energy release rate under mixed mode conditions would require the use of a 3-D interaction integral, which is beyond the scope of the current work. For cycles 2 to 4, the J-integral strain energy release rate calculated with the assumption of linear elasticity is substantially higher than the one calculated with the strain dependent UMAT. The respective average values are of 424 ± 47 J m^{-2} and 190 ± 25 J m^{-2} (i.e. Fig. 13). With the strain dependent UMAT, the predicted stresses are quite consistent with the diffraction measurements, thus giving higher confidence in the J-integral values determined via this route.

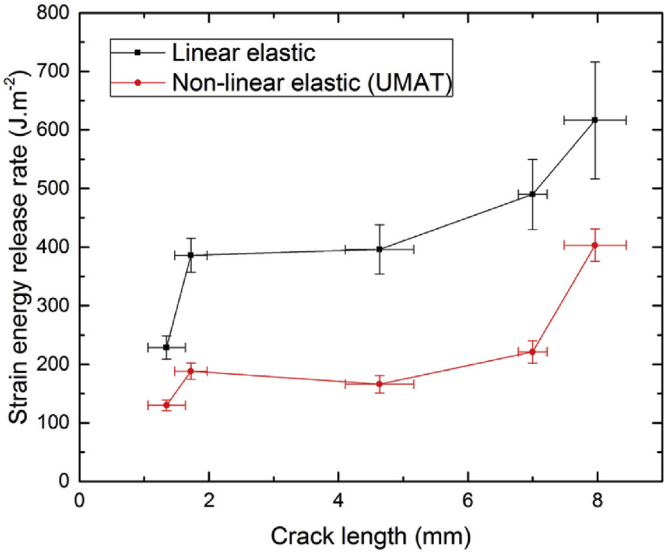

Fig. 13. Strain energy release rate determined as a J-integral as a function of the crack length, which was determined via visual observation of the tomographs. The y-error bar is the standard deviation of the J-integral values along the crack front. (A colour version of this figure can be viewed online.)

When the J value is obtained using an inelastic material law it seems erroneous to use the undamaged bulk elastic modulus to convert J to K. Because of this, K_c values are not presented. However, a nominal K_c can be determined using the undamaged bulk elastic modulus and the standard linear elastic relationships.

6. Discussion

Previous studies of fracture propagation in Gilsocarbon graphite have reported a range of values of fracture propagation resistance. Direct measurements of the work of fracture, via the change in specimen compliance with crack length in compact tension specimens [18], obtained a fracture resistance that rose from 100 to 400 J m^{-2} as the crack extended up to 30 mm in length. Computed tomographs showed the crack front was bowed and bridged by substantial ligaments of material. Such significant bridging may introduce a mechanical shielding effect that could contribute significantly to the apparent fracture resistance [36]. Crack bowing could also lead to errors in the assessment of crack length, and the consequent work of fracture, and this may have affected some earlier studies of Gilsocarbon graphite [13,76] that relied on surface observations. Significant crack bowing was avoided in studies of Gilsocarbon that used double-torsion specimens [12], in which the fracture resistance to propagate the crack, measured over distances up to 50 mm, reached a plateau of 500 J m^{-2}. Its separation into the elastic strain energy release rate and the non-linear inelastic work, by analysis of the load-displacement traces following the method of Sakai [77], showed the elastic energy component was constant at around 250 J m^{-2}. More recently, direct measurements of the total work of fracture in chevron-notched specimens of Gilsocarbon graphite [78], reported values of between 200 and 300 J m^{-2}, with an increase with specimen size. Small chevron specimens do not develop significant inelastic deformation or crack bridging, so their total fracture energy would be expected to approach the intrinsic

toughness of the microstructure. The critical elastic strain energy release rate was calculated directly from the crack field in this study (Fig. 13), and its value of approximately 200 J m^{-2} is quite consistent with the independent measurements obtained in the same material. It measures the intrinsic fracture resistance of the microstructure, as graphite is a quasi-brittle material that exhibits no significant plastic deformation. The intrinsic fracture resistance, which is calculated from the crack field, is expected to be independent of size. However, the total fracture resistance also includes the extrinsic contributions from the development of redundant microcracking in the specimen that does not contribute directly to crack propagation, and crack wake processes such as bridging. Both may depend on the specimen and crack geometry, and so will introduce size dependence. Wake processes that depend on friction may also be sensitive to the mode of crack loading [79].

In summary, the analysis of the experimental data presented in this paper shows that the mode I elastic strain energy release rate in the crack tip field provides a satisfactory fracture propagation criterion for polygranular graphite. Direct analysis of the crack field, as done in this work, serves to measure the intrinsic fracture resistance of the microstructure. To predict unstable fracture propagation in engineering components, and to assess material properties from fracture analyses, it would be important to account also for the redundant damage and residual strains in the microstructure and other extrinsic factors that can increase the apparent work of fracture.

7. Conclusions

- Tensile strain reduces the elastic properties of polygranular nuclear graphite, and this reduces the stress field at the crack tip. This has been demonstrated by synchrotron X-ray tomography, analysed by digital volume correlation, and synchrotron X-ray diffraction to map the total strain and elastic strain fields of a statically loaded crack.
- Finite element simulation, with a suitable material law and directly measured boundary conditions of the deformation acting on the crack, can be used to calculate the elastic strain field, which can be expressed as a J-integral. The value obtained for a mode I crack that is in static equilibrium is the intrinsic fracture resistance of polygranular nuclear graphite.
- A method has been presented that permits a direct comparison between the measured elastic strains of the crack field, with those calculated from the measured displacement field. This may have utility in other situations such as the effects of residual stress on fracture and fatigue.

Acknowledgments

Dr Luis Saucedo Mora and Prof. James Marrow were supported by the UK Engineering and Physical Science Research Council (EPSRC) under grant EP/J01992/1 (QUBE: QUasi-Brittle fracture: a 3D Experimentally-validated approach). Prof. James Marrow and Dr Mahmoud Mostafavi also gratefully acknowledge the support of the Oxford Martin School (Nuclear Programme). Birmingham University (Prof. Brian Connolly) is thanked for the loan of the loading rig, which was provided via EPSRC Grant (EP/H025286/1: Long Term, In Situ Material Degradation Studies Utilizing High Resolution Laboratory X-ray Tomography). The Diamond Light Source synchrotron is acknowledged for the award of beam time under experiment EE9478. The support of Mr Matthew Jordan by EDF Energy Generation, that also provided the material, is gratefully acknowledged (EPSRC Industrial CASE studentship 11220486). Mr Selim Barhli was supported by Department of Materials Engineering and Physical Sciences Research Council (EPSRC) Doctoral Training Account (studentship 1382829); he and Mr Ahmet Cinar acknowledge their support by LaVision Gbmh. The authors thank Mr Henry Lawrence (Magdelen College School) for performing the manual crack measurements from X-ray tomographs, and Dr Fabien Leonard (University of Manchester) and Mr Chung-Roung Zou (National University of Defense Technology, PR China) for their assistance with data collection at the Diamond Light Source. Data may be obtained from the corresponding author.

Appendix A. Supplementary data

Supplementary data related to this article can be found at http://dx.doi.org/10.1016/j.carbon.2017.08.075.

References

[1] B.T. Kelly, Graphite—the most fascinating nuclear material, Carbon N. Y. 20 (1982) 3–11, http://dx.doi.org/10.1016/0008-6223(82)90066-5.
[2] B.J. Marsden, G.N. Hall, Graphite in gas-cooled reactors, in: R.J.M. Konings (Ed.), Compr. Nucl. Mater., Elsevier Ltd, 2012, pp. 325–390, http://dx.doi.org/10.1016/B978-0-08-056033-5.00092-6.
[3] J.-P. Bonal, A. Kohyama, J. van der Laan, L.L. Snead, Graphite, ceramics, and ceramic composites for high-temperature nuclear power systems, MRS Bull. 34 (2009) 28–34, http://dx.doi.org/10.1557/mrs2009.9.
[4] M.P. Hindley, D.C. Blaine, A.A. Groenwold, T.H. Becker, Failure prediction of full-size reactor components from tensile specimen data on NBG-18 nuclear graphite, Nucl. Eng. Des. 284 (2015) 1–9, http://dx.doi.org/10.1016/j.nucengdes.2014.12.011.
[5] M.R. Ayatollahi, F. Berto, P. Lazzarin, Mixed mode brittle fracture of sharp and blunt V-notches in polycrystalline graphite, Carbon N. Y. 49 (2011) 2465–2474, http://dx.doi.org/10.1016/j.carbon.2011.02.015.
[6] M.R. Ayatollahi, A.R. Torabi, Tensile fracture in notched polycrystalline graphite specimens, Carbon N. Y. 48 (2010) 2255–2265, http://dx.doi.org/10.1016/j.carbon.2010.02.041.
[7] T.D. Burchell, A microstructurally based fracture model for polygranular graphites, Carbon N. Y. 34 (1996) 297–316, http://dx.doi.org/10.1016/0008-6223(95)00171-9.
[8] M.O. Tucker, N. McLachlan, Fracture and microstructure of graphites, J. Phys. D. Appl. Phys. 26 (1993) 893–907, http://dx.doi.org/10.1088/0022-3727/26/6/001.
[9] G.B. Neighbour, B. McEnaney, M. Phillips, Acoustic emission responses from cyclic loading of a nuclear graphite, Carbon N. Y. 30 (1992) 359–363, http://dx.doi.org/10.1016/0008-6223(92)90031-Q.
[10] T.J. Marrow, D. Liu, S.M. Barhli, L. Saucedo Mora, Y. Vertyagina, D.M. Collins, C. Reinhard, S. Kabra, P.E.J. Flewitt, D.J. Smith, In situ measurement of the strains within a mechanically loaded polygranular graphite, Carbon N. Y. 96 (2016) 285–302, http://dx.doi.org/10.1016/j.carbon.2015.09.058.
[11] R. Taylor, R.G. Brown, K. Gilchrist, E. Hall, A.T. Hodds, B.T. Kelly, F. Morris, The mechanical properties of reactor graphite, Carbon N. Y. 5 (1967) 519–531.
[12] T.H. Becker, T.J. Marrow, R.B. Tait, Damage, crack growth and fracture characteristics of nuclear grade graphite using the double torsion technique, J. Nucl. Mater. 414 (2011) 32–43, http://dx.doi.org/10.1016/j.jnucmat.2011.04.058.
[13] P. Ouagne, G.B. Neighbour, B. McEnaney, Crack growth resistance in nuclear graphites, J. Phys. D. Appl. Phys. 35 (2002) 927, http://dx.doi.org/10.1088/0022-3727/35/9/315.
[14] A.R. Shahani, M.M. Nejadi, Investigation on the mechanical properties and fracture toughness of graphite, Fatig. Fract. Eng. Mater. Struct. 38 (2015) 1209–1218, http://dx.doi.org/10.1111/ffe.12300.
[15] M. Mostafavi, S.A. McDonald, P.M. Mummery, T.J. Marrow, Observation and quantification of three-dimensional crack propagation in poly-granular graphite, Eng. Fract. Mech. 110 (2013) 410–420, http://dx.doi.org/10.1016/j.engfracmech.2012.11.023.
[16] J.E. Brocklehurst, M.I. Darby, Concerning the fracture of graphite under different test conditions, Mater. Sci. Eng. 16 (1974) 91–106, http://dx.doi.org/10.1016/0025-5416(74)90143-8.
[17] P.-Y. Tang, Interpretation of bend strength increase of graphite by the couple-stress theory, Comput. Struct. 16 (1983) 45–49, http://dx.doi.org/10.1016/0045-7949(83)90146-3.
[18] A. Hodgkins, T.J. Marrow, P. Mummery, B. Marsden, A. Fok, X-ray tomography observation of crack propagation in nuclear graphite, Mater. Sci. Technol. 22 (2006) 1045–1051, http://dx.doi.org/10.1179/174328406X114126.
[19] F. Berto, P. Lazzarin, C. Marangon, Brittle fracture of U-notched graphite plates under mixed mode loading, Mater. Des. 41 (2012) 421–432, http://dx.doi.org/10.1016/j.matdes.2012.05.022.
[20] H. Li, J. Duff, T.J. Marrow, In-situ observation of crack nucleation in nuclear graphite by digital image correlation, Mater. Fabr. 6 (2008) 813–820, http://dx.doi.org/10.1115/PVP2008-61136.
[21] M. Mostafavi, T.J. Marrow, In situ observation of crack nuclei in poly-granular graphite under ring-on-ring equi-biaxial and flexural loading, Eng. Fract.

Mech. 78 (2011) 1756–1770, http://dx.doi.org/10.1016/j.engfracmech.2010.11.004.
[22] M. Mostafavi, T.J. Marrow, Quantitative in situ study of short crack propagation in polygranular graphite by digital image correlation, Fatig. Fract. Eng. Mater. Struct. 35 (2012) 695–707, http://dx.doi.org/10.1111/j.1460-2695.2012.01648.x.
[23] M.R. Joyce, T.J. Marrow, Microstructural scale strain localisation in nuclear graphite, J. Nucl. Mater. 381 (2008) 171–176, http://dx.doi.org/10.1016/j.jnucmat.2008.07.013.
[24] S.R. McNeill, W.H. Peters, M.A. Sutton, Estimation of stress intensity factor by digital image correlation, Eng. Fract. Mech. 28 (1987).
[25] M.S. Kirugulige, H.V. Tippur, Measurement of fracture parameters for a mixed-mode crack driven by stress waves using image correlation technique and high-speed digital photography, Strain 45 (2009) 108–122, http://dx.doi.org/10.1111/j.1475-1305.2008.00449.x.
[26] T.H. Becker, M. Mostafavi, R.B. Tait, T.J. Marrow, An approach to calculate the J-integral by digital image correlation displacement field measurement, Fatig. Fract. Eng. Mater. Struct. 35 (2012) 971–984, http://dx.doi.org/10.1111/j.1460-2695.2012.01685.x.
[27] O. Kolednik, On the physical meaning of the J-δa-curves, Eng. Fract. Mech. 38 (1991) 403–412, http://dx.doi.org/10.1016/0013-7944(91)90092-F.
[28] M.C. Walters, G.H. Paulino, R.H. Dodds, Interaction integral procedures for 3-D curved cracks including surface tractions, Eng. Fract. Mech. 72 (2005) 1635–1663, http://dx.doi.org/10.1016/j.engfracmech.2005.01.002.
[29] A.J. Allen, M.T. Hutchings, C.G. Windsor, C. Andreani, Neutron diffraction methods for the study of residual stress fields, Adv. Phys. 34 (1985) 445–473, http://dx.doi.org/10.1080/00018738500101791.
[30] P.J. Withers, P.J. Webster, Neutron and synchrotron x-ray strain scanning, Strain 37 (2001) 19–33, http://dx.doi.org/10.1111/j.1475-1305.2001.tb01216.x.
[31] R.A. Young, The Rietveld Method, International Union of Crystallography/Oxford University Press, Oxford, 1993, http://dx.doi.org/10.1002/crat.2170300412.
[32] P. Lopez-Crespo, M. Mostafavi, A. Steuwer, J.F. Kelleher, T. Buslaps, P.J. Withers, Characterisation of overloads in fatigue by 2D strain mapping at the surface and in the bulk, Fatig. Fract. Eng. Mater. Struct. 39 (2016), http://dx.doi.org/10.1111/ffe.12463.
[33] J.E. Allison, Measurement of crack-tip stress distributions by x-ray diffraction, in: Fract. Mech. Proc. Elev. Natl. Symp. Fract. Mech., ASTM STP677, 1979.
[34] R.A. Owen, R. V Preston, P.J. Withers, H.R. Shercliff, P.J. Webster, Neutron and synchrotron measurements of residual strain in TIG welded aluminium alloy 2024, Mater. Sci. Eng. A 346 (2003) 159–167.
[35] A.J. Allen, M.A.M. Bourke, S. Dawes, M.T. Hutchings, P.J. Withers, The analysis of internal strains measured by neutron diffraction in Al/SiC metal matrix composites, Acta Metall. Mater. 40 (1992) 2361–2373, http://dx.doi.org/10.1016/0956-7151(92)90155-8.
[36] T.J. Marrow, A. Steuwer, F. Mohammed, D. Engelberg, M. Sarwar, Measurement of crack bridging stresses in environment-assisted cracking of duplex stainless by synchrotron diffraction, Fract. Eng. Mater. Struct. 29 (2006) 464–471, http://dx.doi.org/10.1111/j.1460-2695.2006.01019.x.
[37] J.P. Belnoue, T.-S. Jun, F. Hofmann, B. Abbey, A.M. Korsunsky, Evaluation of the overload effect on fatigue crack growth with the help of synchrotron XRD strain mapping, Eng. Fract. Mech. 77 (2010) 3216–3226, http://dx.doi.org/10.1016/j.engfracmech.2010.08.018.
[38] S.M. Barhli, L. Saucedo Mora, C. Simpson, M. Mostafavi, P.J. Withers, T.J. Marrow, Obtaining the J-integral by diffraction-based crack-field strain mapping, in: Procedia Struct. Integr., Catania, Italy, 2016, pp. 2519–2526.
[39] A. Hodgkins, T.J. Marrow, M.R. Wootton, R. Moskovic, P.E.J. Flewitt, Fracture behaviour of radiolytically oxidised reactor core graphites: a view, Mater. Sci. Technol. 26 (2010) 899–907, http://dx.doi.org/10.1179/026708309X12526555493477.
[40] B.L. Karihaloo, H.M. Abdalla, Q.Z. Xiao, Deterministic size effect in the strength of cracked concrete structures, Cem. Concr. Res. 36 (2006) 171–188, http://dx.doi.org/10.1016/j.cemconres.2005.04.007.
[41] M. Mostafavi, N. Baimpas, E. Tarleton, R.C. Atwood, S.A. McDonald, A.M. Korsunsky, T.J. Marrow, Three-dimensional crack observation, quantification and simulation in a quasi-brittle material, Acta Mater. 61 (2013) 6276–6289, http://dx.doi.org/10.1016/j.actamat.2013.07.011.
[42] V. Veselý, P. Frantík, An application for the fracture characterisation of quasi-brittle materials taking into account fracture process zone influence, Adv. Eng. Softw. 72 (2014) 66–76, http://dx.doi.org/10.1016/j.advengsoft.2013.06.004.
[43] A.L. Rosa, R.C. Yu, G. Ruiz, L. Saucedo, J.L.A.O. Sousa, A loading rate dependent cohesive model for concrete fracture, Eng. Fract. Mech. 82 (2012) 195–208, http://dx.doi.org/10.1016/j.engfracmech.2011.12.013.
[44] A.R. Ingraffea, V. Saouma, Numerical modeling of discrete crack propagation in reinforced and plain concrete, in: Fract. Mech. Concr. Struct. Appl. Numer. Calc., Springer, Netherlands, Dordrecht, 1985, pp. 171–225, http://dx.doi.org/10.1007/978-94-009-6152-4_4.
[45] Z. Zou, S.L. Fok, B.J. Marsden, S.O. Oyadiji, Numerical simulation of strength test on graphite moderator bricks using a continuum damage mechanics model, Eng. Fract. Mech. 73 (2006) 318–330, http://dx.doi.org/10.1016/j.engfracmech.2005.08.002.
[46] L. Saucedo-Mora, C. Zou, T. Lowe, T.J. Marrow, Three-dimensional measurement and cohesive element modelling of deformation and damage in a 2.5-dimensional woven ceramic matrix composite, Fatig. Fract. Eng. Mater. Struct. (2016), http://dx.doi.org/10.1111/ffe.12537.
[47] R. Moskovic, Degradation of graphite in gas cooled reactors due to radiolytic oxidation, Nucl. Eng. Des. 269 (2014) 83–87, http://dx.doi.org/10.1016/j.nucengdes.2013.08.011.
[48] S. Sato, A. Kurumada, K. Kawamata, T. Takizawa, K. Teruyama, Neutron irradiation effects on thermal shock resistance and fracture toughness of graphites as plasma-facing first wall components for fusion reactor devices, Carbon N. Y. 27 (1989) 507–516, http://dx.doi.org/10.1016/0008-6223(89)90001-8.
[49] M.M. Mirsayar, F. Berto, M.R.M. Aliha, P. Park, Strain-based criteria for mixed-mode fracture of polycrystalline graphite, Eng. Fract. Mech. 156 (2016) 114–123, http://dx.doi.org/10.1016/j.engfracmech.2016.02.011.
[50] S.R. Stock, X-ray microtomography of materials, Int. Mater. Rev. 44 (1999) 141–164, http://dx.doi.org/10.1179/095066099101528261.
[51] E. Maire, J.Y. Buffière, L. Salvo, J.J. Blandin, W. Ludwig, J.M. Létang, On the application of x-ray microtomography in the field of materials science, Adv. Eng. Mater. 3 (2001) 539, http://dx.doi.org/10.1002/1527-2648(200108)3:8<539::AID-ADEM539>3.0.CO;2–6.
[52] T.J. Marrow, J.Y. Buffiere, P.J. Withers, G. Johnson, D. Engelberg, High resolution X-ray tomography of short fatigue crack nucleation in austempered ductile cast iron, Int. J. Fatig. 26 (2004) 717–725, http://dx.doi.org/10.1016/j.ijfatigue.2003.11.001.
[53] L. Saucedo-Mora, T. Lowe, S. Zhao, P.D. Lee, P.M. Mummery, T.J. Marrow, In situ observation of mechanical damage within a SiC-SiC ceramic matrix composite, J. Nucl. Mater. 481 (2016) 13–23, http://dx.doi.org/10.1016/j.jnucmat.2016.09.007.
[54] B.K. Bay, T.S. Smith, D.P. Fyhrie, M. Saad, Digital volume correlation: three-dimensional strain mapping using X-ray tomography, Exp. Mech. 39 (1999) 217–226, http://dx.doi.org/10.1007/BF02323555.
[55] A. Steuwer, L. Edwards, S. Pratihar, S. Ganguly, M. Peel, M.E. Fitzpatrick, T.J. Marrow, P.J. Withers, I. Sinclair, K.D. Singh, N. Gao, T. Buslaps, J.Y. Buffière, In situ analysis of cracks in structural materials using synchrotron X-ray tomography and diffraction, Nucl. Instrum. Meth. Phys. Res. Sect. B Beam Interact. Mater. Atoms 246 (2006) 217–225, http://dx.doi.org/10.1016/j.nimb.2005.12.063.
[56] J. Réthoré, N. Limodin, J.Y. Buffiere, F. Hild, W. Ludwig, S. Roux, Digital volume correlation analyses of synchrotron tomographic images, J. Strain Anal. Eng. Des. 46 (2011) 683–695, http://dx.doi.org/10.1177/0309324711409999.
[57] F. Forsberg, C.R. Siviour, 3D deformation and strain analysis in compacted sugar using x-ray microtomography and digital volume correlation, Meas. Sci. Technol. 20 (2009) 95703, http://dx.doi.org/10.1088/0957-0233/20/9/095703.
[58] Y. Barranger, P. Doumalin, J.C. Dupre, A. Germaneau, S. Hedan, V. Valle, Evaluation of three-dimensional and two-dimensional full displacement fields of a single edge notch fracture mechanics specimen, in light of experimental data using X-ray tomography, Eng. Fract. Mech. 76 (2009) 2371–2383, http://dx.doi.org/10.1016/j.engfracmech.2009.08.001.
[59] M. Mostafavi, Y. Vertyagina, C. Reinhard, R. Bradley, X. Jiang, M. Galano, J. Marrow, 3D Studies of Indentation by Combined X-ray Tomography and Digital Volume Correlation, in: 13th Eur. Conf. Fract. Key Eng. Mater., Brno, Czech Republic, 2013.
[60] M. Mostafavi, R. Bradley, D.E.J. Armstrong, T.J. Marrow, Quantifying yield behaviour in metals by X-ray nanotomography, Sci. Rep. 6 (2016) 34346, http://dx.doi.org/10.1038/srep34346.
[61] M.S.L. Jordan, L. Saucedo-Mora, S.M. Barhli, D. Nowell, T.J. Marrow, Measurements of Stress Concentration Behaviour in AGR Nuclear Graphite, in: 23 Rd Conf. Struct. Mech. React. Technol., Manchester, UK, 2015.
[62] S.D. Preston, B.J. Marsden, Changes in the coefficient of thermal expansion in stressed Gilsocarbon graphite, Carbon N. Y. 44 (2006) 1250–1257, http://dx.doi.org/10.1016/j.carbon.2005.10.045.
[63] M. Drakopoulos, T. Connolley, C. Reinhard, R. Atwood, O. Magdysyuk, N. Vo, M. Hart, L. Connor, B. Humphreys, G. Howell, S. Davies, T. Hill, G. Wilkin, U. Pedersen, A. Foster, N. De Maio, M. Basham, F. Yuan, K. Wanelik, I12: the Joint engineering, environment and processing (JEEP) beamline at Diamond light Source, J. Synchrotron Radiat. 22 (2015) 828–838, http://dx.doi.org/10.1107/S1600577515003513.
[64] S. Titarenko, P.J. Withers, A. Yagola, An analytical formula for ring artefact suppression in X-ray tomography, Appl. Math. Lett. 23 (2010) 1489–1495, http://dx.doi.org/10.1016/j.aml.2010.08.022.
[65] C.A. Schneider, W.S. Rasband, K.W. Eliceiri, NIH Image to ImageJ: 25 years of image analysis, Nat. Meth. 9 (2012) 671–675, http://dx.doi.org/10.1038/nmeth.2089.
[66] K. Wen, J. Marrow, B. Marsden, Microcracks in nuclear graphite and highly oriented pyrolytic graphite (HOPG), J. Nucl. Mater. 381 (2008) 199–203, http://dx.doi.org/10.1016/j.jnucmat.2008.07.012.
[67] A.F. Cinar, S.M. Barhli, D. Hollis, M. Flansbjer, R.A. Tomlinson, T.J. Marrow, M. Mostafavi, An autonomous surface discontinuity detection and quantification method by digital image correlation and phase congruency, Opt. Lasers Eng. 96 (2017).
[68] ASTM International, ASTM E647-15e1 Standard Test Method for Measurement of Fatigue Crack Growth Rates, 2015.
[69] M.O. Tucker, A.P.G. Rose, T.D. Burchell, The fracture of polygranular graphites, Carbon N. Y. 24 (1986) 581–602, http://dx.doi.org/10.1016/0008-6223(86)90149-1.
[70] A.P.G. Rose, M.O. Tucker, A fracture criterion for nuclear graphite, J. Nucl. Mater. 110 (1982) 186–195, http://dx.doi.org/10.1016/0022-3115(82)90145-3.

[71] J.R. Rice, A path independent integral and the approximate analysis of strain concentration by notches and cracks, J. Appl. Mech. 35 (1968) 379–386.
[72] S.M. Barhli, M. Mostafavi, A.F. Cinar, D. Hollis, T.J. Marrow, J-integral calculation by finite element processing of measured full-field surface displacements, Exp. Mech. (2017) 1–13, http://dx.doi.org/10.1007/s11340-017-0275-1.
[73] H. Wendland, Scattered Data Approximation, Cambridge University Press, Cambridge, 2005, http://dx.doi.org/10.2277/0521843359.
[74] J. Poissant, F. Barthelat, A novel 'Subset splitting' procedure for digital image correlation on discontinuous displacement fields, Exp. Mech. 50 (2009) 353–364, http://dx.doi.org/10.1007/s11340-009-9220-2.
[75] D.M. Parks, The Virtual Crack Extension method for non linear material behavior, Comput. Meth. Appl. Mech. Eng. 12 (1977) 353–364.
[76] S. Fazluddin, Crack Growth Resistance in Nuclear Graphite, University of Leeds, 2002.
[77] M. Sakai, J. Yoshimura, Y. Goto, M. Inagaki, R-Curve behavior of a polycrystalline graphite: microcracking and grain bridging in the wake region, J. Am. Ceram. Soc. 71 (1988) 609–616, http://dx.doi.org/10.1111/j.1151-2916.1988.tb06377.x.
[78] N. Tzelepi, P. Ramsay, Development of new techniques for AGR graphite, 4th EDF Energy Nucl. Graph. Symp. Eng. Challenges Assoc. Life Graph. React. Cores (2015) 397–412. Nottingham, UK.
[79] H.M. Jensen, Mixed mode interface fracture criteria, Acta Metall. Mater. 38 (1990) 2637–2644, http://dx.doi.org/10.1016/0956-7151(90)90276-M.